Available online at www.sciencedirect.com
SCIENCE DIRECT
Electric Power Systems Research 76 (2006) 729–741
ELECTRIC POWER SYSTEMS RESEARCH
www.elsevier.com/locate/epsr

Advanced design methodology for single and dual voltage wound core power transformers based on a particular finite element model

Marina A. Tsili [a], Antonios G. Kladas [a,*], Pavlos S. Georgilakis [b], Athanasios T. Souflaris [c], Dimitris G. Paparigas [c]

[a] *Faculty of Electrical & Computer Engineering, National Technical University of Athens, GR-15780, Athens, Greece*
[b] *Department of Production Engineering and Management, Technical University of Crete, GR-73100, Chania, Greece*
[c] *Schneider Electric AE, Elvim Plant, GR-32011, Inofyta, Viotia, Greece*

Received 10 January 2005; received in revised form 3 August 2005; accepted 8 September 2005
Available online 27 December 2005

Abstract

The paper presents an accurate and cost effective three-dimensional finite element model for the analysis and design of wound core, shell type, power transformers, focusing on the short-circuit impedance evaluation. The model efficiency lies on the detailed representation of the transformer geometry along with the adoption of a particular reduced scalar potential formulation enabling three-dimensional magnetostatic problem solution without prior source field calculation. Its accuracy is validated through local field measurements and through comparison of the calculated short-circuit impedance value with the measured one for several commercial wound core, shell type transformers. In such transformers, involving extensive winding parts out of the core window, the detailed representation of the transformer geometry, including the winding cooling ducts, provides accurate results for low densities of the three-dimensional finite element mesh, resulting to reduction of the required calculation time. The model is used in the development of a computational tool, which enables the automated and accurate transformer characteristics prediction, adopted to the manufacturing process. This tool has also been applied in the impedance calculation for different winding connections of dual voltage transformers, thus providing the information needed for the achievement of an accurate design and the enhancement of the manufacturer's ability to reduce design margins. The methodology presented in this paper has been incorporated in the design process of a transformer manufacturing industry.

Keywords: Finite element method; Power transformers; Transformer windings; Dual voltage; Short-circuit impedance

1. Introduction

In the light of 21st century energy market, where competition continues to accelerate in the electric industry, utilities will try to further improve system reliability and quality, while simultaneously being cost effective. The transformer manufacturing industry must improve transformer efficiency and reliability while reducing cost, since high quality, low cost products have become the key to survival [1,2]. Transformer efficiency is improved by reducing load and no-load losses. Transformer reliability is mainly improved by the accurate evaluation of the leakage field, the short-circuit impedance and the resulting forces on transformer windings under short-circuit, since these enable to avoid mechanical damages and failures during short-circuit tests and power system faults.

The transformer users specify a desired level of load losses, no-load losses and short-circuit impedance (specified values). It is within the transformer designer responsibilities to implement the transformer design so as the transformer to meet the specified values at the lowest cost. The transformer is designed so that its losses and short-circuit impedance (designed values) are very close to the specified ones, while a design margin is used since, in practice, transformer measured losses and short-circuit impedance deviate from the designed ones due to constructional and measurement tolerances. The transformer manufacturer guarantees the values of losses and short-circuit impedance (guaranteed values), while the permissible deviations of the guaranteed values from the measured ones are specified

* Corresponding author. Tel.: +30 210 7723765; fax: +30 210 7722336.
E-mail addresses: kladasel@central.ntua.gr (A.G. Kladas), pgeorg@dpem.tuc.gr (P.S. Georgilakis), dimitris.paparigas@gr.schneider-electric.com (D.G. Paparigas).

0378-7796/$ – see front matter © 2005 Elsevier B.V. All rights reserved.
doi:10.1016/j.epsr.2005.09.019

by international standards [3] and the transformer manufacturers are obliged to comply with them.

Accurate estimation of transformer losses and short-circuit impedance during the transformer design phase is crucial, since,

(1) it increases transformer reliability and manufacturer credibility;
(2) it secures the desired transformer efficiency;
(3) it reduces the material cost, since smaller design margin is used;
(4) it decreases transformer delivery time, since there is no need for transformer prototype (to confirm the accuracy of transformer design) as well as for short-circuit tests under nominal voltage (which are very laborious and expensive).

However, some of the existing design methodologies used by manufacturers still rely on leakage field and short-circuit impedance calculations that include gross approximations and assumptions and incorporate empirical factors in the transformer magnetic field simulation. This approach is likely to result into significant deviations from the measured short-circuit impedance values, augmenting the risk of transformer failure and overstepping of the respective guaranteed values. It is therefore necessary to develop improved methods of leakage field evaluation, incorporable to the transformer design process. For this purpose, research effort in this field focuses on the use of advanced power transformer modeling techniques that take into account the constructional details of these devices.

Numerical modeling techniques consist some of the most widely used tools for electrical machines analysis, as they have proven their effectiveness in the representation of all their important features. The finite element method (FEM) has been extensively applied in the calculation of equivalent circuit parameters of synchronous machines [4], as well as induction motors [5] and generators [6]. Special machines as permanent magnet [7,8] or switched reluctance machines [9] have also been analyzed with the use of this numerical method. Two-dimensional (2D) and three-dimensional (3D) FEM models are widely encountered in the technical literature, for the calculation of transformer leakage field [10], losses [11] and forces during short-circuit [12]. Moreover, non-linear laminated iron characteristics have been appropriately represented [13,14] as well as power transformers interaction with non-linear loads has been simulated by using coupling of field and circuits equations [15,16].

Accurate prediction of power transformer characteristics requires, in general, 3D FEM models involving a large number of unknowns and resulting frequently in laborious and expensive numerical schemes. A possibility to reduce the number of degrees of freedom is offered by adopting hybrid numerical techniques [17]. However, this increases the model complexity, and is rather advantageous in checking the transformer parameters at the final design stage. At the preliminary design stages, it is preferable to use a FEM model adopting some geometrical simplifications for the transformer geometry, enabling to reduce substantially the number of unknowns. However, due to these approximations, significant deviations from test results are likely to appear and model modifications may be needed to accurately predict the examined characteristics. The present paper aims to contribute to this direction, by introducing a detailed transformer 3D FEM model, able to give accurate leakage field results for low mesh densities. In this model, which applies to single and dual voltage power transformers, a particular reduced scalar potential formulation is adopted, reducing significantly the computational effort of the magnetic field sources calculation. This formulation, in conjunction with the detailed modeling of the transformer windings, including the modeling of cooling ducts, results to a computational tool, which allows the accurate and fast prediction of the transformer short-circuit impedance. Such a technique is particularly important for wound core, shell type transformers representation, involving extensive winding parts out of the core window. Comparisons between the results of the proposed method and measured values are presented for a number of commercial transformers, proving its validity and accuracy. The model is also used in the development of a computer code, which implements the short-circuit impedance calculation for use in the transformer manufacturing industry during the design process.

The paper is organized as follows: Section 2 describes the developed FEM models for the transformer magnetic field analysis. A comparative presentation of their results on several transformer cases is given in Section 3 along with the presentation of the computational tool based on the models and its application to the impedance prediction for different winding arrangements in dual voltage transformers. Finally, Section 4 concludes the paper.

2. Transformer modeling by a particular finite element formulation

2.1. Field equations by using a particular reduced scalar potential formulation

The finite element method is a numerical technique for the solution of problems described by partial differential equations. The governing equation in the case of a magnetostatic field is the Laplace equation:

$$\nabla^2 \Phi_m = 0 \tag{1}$$

where Φ_m is the scalar magnetic potential. The considered field is represented by a group of finite elements. The space discretization is realized by triangles or tetrahedra if the problem is two- or three-dimensional, respectively. Therefore, a continuous physical problem is converted into a discrete problem of finite elements with unknown field values in their vertices nodes. The solution of such a problem reduces into a system of algebraic equations and the field values inside the elements can be retrieved with the use of calculated values in their indices.

Many scalar potential formulations have been developed for 3D magnetostatics, but they usually necessitate a prior source field calculation by using Biot–Savart's law. This presents the drawback of considerable computational effort.

In the present paper, a particular scalar potential formulation has been developed, enabling the 3D magnetostatic field

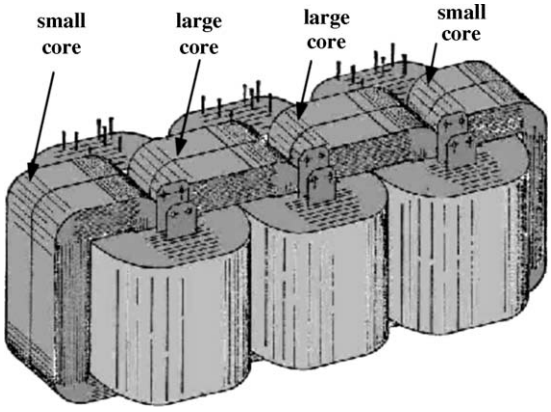

Fig. 1. Active part configuration of the three-phase wound core power transformer considered.

analysis. According to this method, the magnetic field strength **H** is conveniently partitioned to a rotational and an irrotational part as follows:

$$\mathbf{H} = \mathbf{K} - \nabla\Phi \tag{2}$$

where Φ is a scalar potential extended all over the solution domain, while **K** is a vector quantity (fictitious field distribution) that satisfies the following conditions [18]:

(1) **K** is limited in a simply connected subdomain comprising the conductor;
(2) $\nabla \times \mathbf{K} = \mathbf{J}$ in the conductor and $\nabla \times \mathbf{K} = 0$ outside it;
(3) **K** is perpendicular on the subdomain boundary.

The above formulation satisfies Ampere's law for an arbitrary contour in the subdomain.

2.2. Representation of the transformer configuration

The transformer under consideration is a 630 kVA, rated primary voltages 20 and 15 kV delta connected (dual primary voltage 20–15 kV), rated secondary voltage 400 V star connected, three-phase, wound core, oil-immersed, power transformer, shown in Fig. 1. The secondary winding comprises 16 layers (per phase) of copper sheet, while the primary consists of 1385 turns (per phase) of insulated copper wire. The transformer magnetic circuit is of shell type and is assembled from two small and two large iron wound cores. Fig. 2 illustrates the perspective view of the transformer one-phase part modeled.

The model of Fig. 2 comprises the low voltage (LV) and high voltage (HV) windings of one phase, as well as the small and large iron core that surrounds them. An air box, whose dimensions are equal to the transformer tank dimensions, surrounds the active part, therefore confining the field calculation to this domain. The *xy*-plane of the Cartesian coordinate system used is the transformer symmetry plane, and the *z*-axis crosses the cores symmetry plane. Due to the symmetries of the problem, the solution domain is reduced to one-fourth of the device. These symmetries were taken into account by the imposition of Dirichlet boundary condition ($\Phi = 0$) along *xy*-plane and Neumann

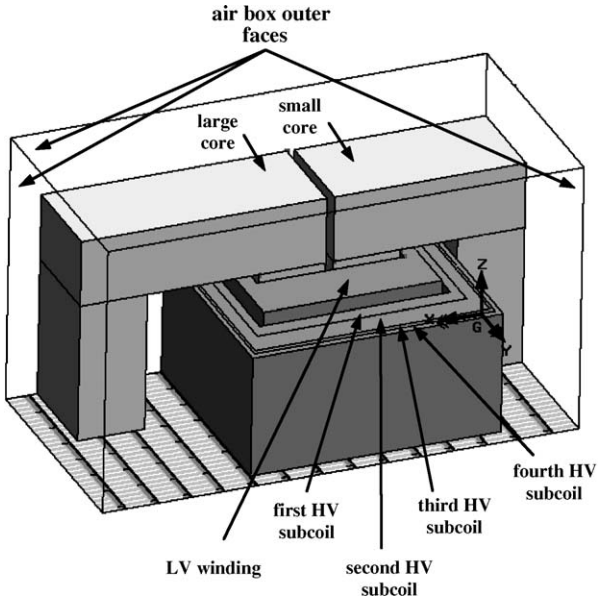

Fig. 2. Perspective view of the transformer one-phase part modeled (simplified winding geometry).

boundary condition ($\frac{\partial\Phi}{\partial n} = 0$) along *yz*-plane, *xz*-plane and the three outer faces of the air box.

The use of this one-phase model instead of the whole three-phase transformer model was conducted for the following reasons:

(i) The smaller model size enables the construction of more dense tetrahedral finite element mesh without great computational cost (given that the exact representation of the transformer magnetic field requires great accuracy which is dependent on the mesh density and the total execution time of the finite element calculations).
(ii) The representation of one phase of the active part does not affect the accuracy of the equivalent circuit parameters calculation.

The HV winding is divided into four subcoils. This division models the winding arrangement that produces the second primary voltage level, shown in Fig. 3. The second one of the four subcoils consists of two sections (HV2a and HV2b) with the same number of turns. When these sections are connected in parallel and then in series with the rest of the HV subcoils, the lower voltage level (15 kV) is obtained. For the production of the higher voltage rating, the two sections (HV2a and HV2b) are connected in series and then in series with the rest of the HV coils. Hence, in the case of the first primary voltage level

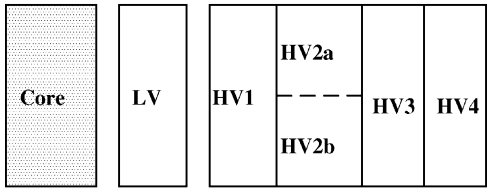

Fig. 3. Winding arrangement (*yz*-plane) for the production of dual primary voltage levels 20–15 kV.

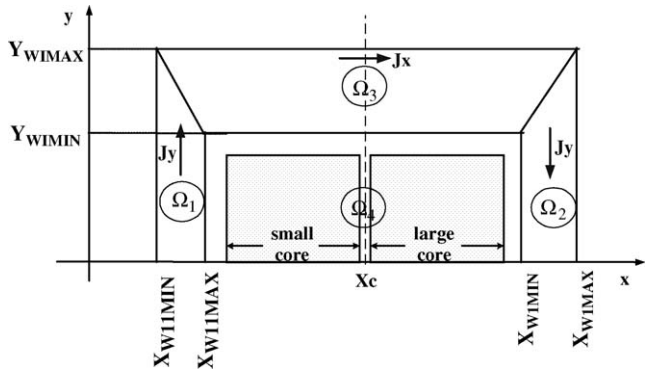

Fig. 4. Regions (xy-plane) of the subdomain used in the calculation of the fictitious field distribution K_z corresponding to the LV winding (orthogonal approximation of the winding corners).

(20 kV) the nominal current is considered to flow through all the subcoils, while in the second one (15 kV), the current of subcoil HV2 (whose sections HV2a and HV2b are connected in parallel) is half of the current flowing through subcoils HV1, HV3 and HV4.

In the FEM model presented in the next sections, the magnetic non-linearity as well as the magnetic anisotropy of the iron cores is ignored. This assumption is justified on the basis that flux densities during short-circuit are very low, therefore confining the transformer operation below the saturation region of the magnetization curve.

2.3. Simplified modeling of the transformer windings

The representation of the magnetic field sources, i.e. the windings current in the case of the transformer magnetic field, is carried out with the use of a fictitious field distribution **K**, which must satisfy the conditions described in Section 2.1. For the calculation of **K**, a simply connected subdomain must be defined for each winding, comprising its conductors. Fig. 4 shows the bottom view of the subdomain corresponding to the LV winding of Fig. 2. This subdomain is divided into four regions (Ω_1, Ω_2, Ω_3 and Ω_4), in order to facilitate the calculation. The symbols shown in Fig. 4 are described in the followings:

X_{W11MIN}, X_{W11MAX}: boundaries of the coil area along x-axis inside the small core window;
X_{W1MIN}, X_{W1MAX}: boundaries of the coil area along x-axis inside the large core window;
Y_{W1MIN}, Y_{W1MAX}: boundaries of the coil area along y-axis;
J_x, J_y: x, y components of winding current density;
X_C: x-coordinate of the winding center.

The calculation of **K** is quite straightforward, given the winding dimensions along x-, y- and z-axes:

(1) *Region Ω_1*: In this region, $J_x = J_z = 0$. The current density J_y is given by:

$$J_y = \mathrm{NI} \cdot \frac{Z}{X_{W11MAX} - X_{W11MIN}} \tag{3}$$

where NI are the ampere turns of LV winding.

The distribution **K** must be perpendicular to Ω_1 boundary (third condition described in Section 2.1). Therefore, it consists of component K_z only, while $K_x = K_y = 0$. The second condition described in Section 2.1 yields:

$$\nabla \times \mathbf{K} = \mathbf{J} \Rightarrow K_z = -\int_{\Omega_1} J_y \, dx$$

$$\Rightarrow K_z = \mathrm{NI} \cdot Z \cdot \frac{X_{W11MIN} - X}{X_{W11MIN} - X_{W11MAX}} \tag{4}$$

(2) *Region Ω_2*: In this region, $J_x = J_z = 0$ and

$$J_y = -\mathrm{NI} \cdot \frac{Z}{X_{W1MAX} - X_{W1MIN}} \tag{5}$$

while K_z derives from:

$$K_z = -\int_{\Omega_2} J_y \, dx = \mathrm{NI} \cdot Z \cdot \frac{X_{W1MAX} - X}{X_{W1MAX} - X_{W1MIN}} \tag{6}$$

(3) *Region Ω_3*: In this region, $J_y = J_z = 0$ and

$$J_x = \mathrm{NI} \cdot \frac{Z}{Y_{W1MAX} - Y_{W1MIN}} \tag{7}$$

Therefore, K_z is given by:

$$K_z = \int_{\Omega_3} J_x \, dy = \mathrm{NI} \cdot Z \cdot \frac{Y_{W1MAX} - Y}{Y_{W1MAX} - Y_{W1MIN}} \tag{8}$$

(4) *Region Ω_4*: The application of continuity boundary condition for K_z between regions Ω_3 and Ω_4 yields:

$$K_z(Y = {Y_{W1MIN}}^-) = K_z(Y = {Y_{W1MIN}}^+)$$

$$\Rightarrow K_z(Y = {Y_{W1MIN}}^-) = \mathrm{NI} \cdot Z \tag{9}$$

The application of continuity boundary condition between regions Ω_1 and Ω_4 or Ω_2 and Ω_4 results to the same equation for K_z in region Ω_4.

Consequently, the overall equation describing the fictitious field distribution corresponding to the LV winding is of the form:

$$K_z = \begin{cases} \mathrm{NI} \cdot Z \cdot \dfrac{X_{W11MIN} - X}{X_{W11MIN} - X_{W11MAX}}, & \text{region } \Omega_1 \\ \mathrm{NI} \cdot Z \cdot \dfrac{X_{W1MAX} - X}{X_{W1MAX} - X_{W1MIN}}, & \text{region } \Omega_2 \\ \mathrm{NI} \cdot Z \cdot \dfrac{Y_{W1MAX} - Y}{Y_{W1MAX} - Y_{W1MIN}}, & \text{region } \Omega_3 \\ \mathrm{NI} \cdot Z, & \text{region } \Omega_4 \end{cases} \tag{10}$$

Fig. 5 gives the 3D graphical representation of K_z component corresponding to LV winding. The symbol Z_{W1MAX} appearing in Fig. 5 denotes the boundary of the coil area along z-axis. Fig. 6 shows the K_z distribution along a plane parallel to y-axis, crossing the center X_c of the winding.

The derivation of distribution **K** for the HV winding is similar, resulting to equation identical to (10), with the respective boundaries of the winding along x-, y- and z-axes.

The representation of current sources through distribution **K** has the advantage of being compatible with the discrete scheme

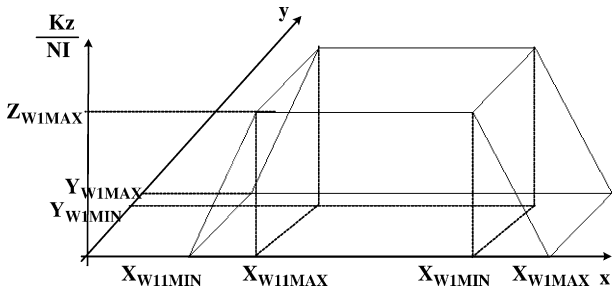

Fig. 5. 3D graphical representation of the fictitious field distribution corresponding to the LV winding of Fig. 2 (orthogonal approximation of the winding corners).

of first-order tetrahedral elements so that it does not suffer from cancellation errors, present in case of using Biot–Savart's law to determine source field distribution.

2.4. Detailed modeling of the transformer windings

The construction of the transformer model with detailed winding geometry is realized in two steps: first, an elliptic approximation of the winding corners is considered, while, afterwards, the winding cooling ducts are inserted into the model.

The simplicity of the calculation of the fictitious field distribution presented in Section 2.3 relies on the orthogonal approximation of the winding corners. However, the real winding geometry is the one shown in Fig. 1. The orthogonal approximation of the winding corners, which are in fact curved, is likely to result to significant overestimation of the current density and the deriving magnetic field density, respectively.

For a more detailed representation of the winding geometry, their corners were considered to be part of ellipses with known center coordinates. Under this consideration, the fictitious field distribution corresponding to the LV winding is the one shown in Fig. 7.

The calculation of the K_z component shown in Fig. 7 is more complicated: the subdomain comprising the LV winding has to be divided into six regions, whose bottom view is shown in Fig. 8, regions Ω_1, Ω_2, Ω_3 and Ω_4 (used in the calculation described in Section 2.3) and regions Ω_5 and Ω_6, which correspond to the

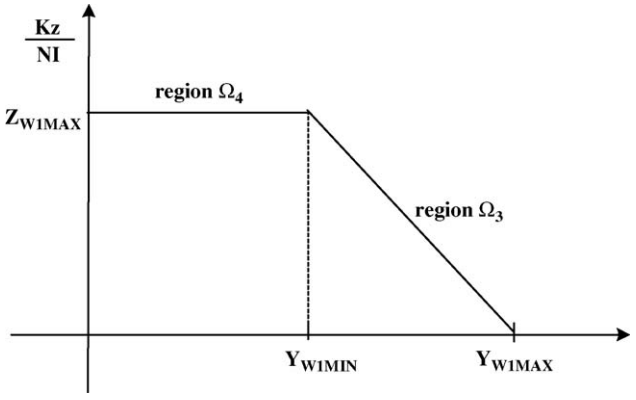

Fig. 6. Fictitious field distribution corresponding to the LV winding along the plane $X = X_c$ of Fig. 4.

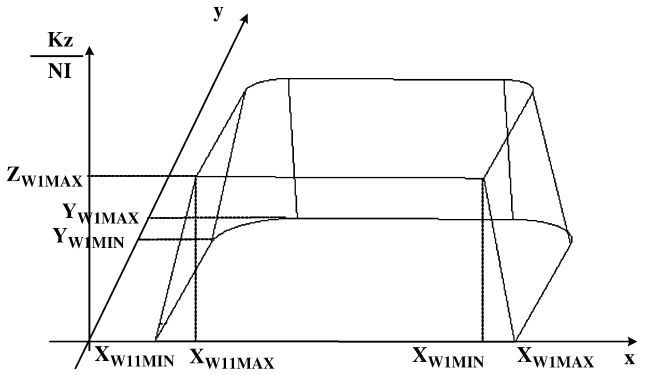

Fig. 7. 3D graphical representation of the fictitious field distribution corresponding to the LV winding of Fig. 1 (elliptical approximation of the winding corners).

winding corners and are bounded by inner ellipses (ε_2), (ε_2') and outer ellipses (ε_1), (ε_1').

In Fig. 8, point (X_o, Y_o) is the center of (ε_1) and (ε_2) while point (X_o', Y_o) is the center of (ε_1') and (ε_2'). The coordinates X_o, X_o' and Y_o derive from the transformer dimensions and can be easily calculated. The equations of the ellipses are:

$$(\varepsilon_1): \frac{(X - X_o)^2 + (Y - Y_o)^2}{(X_{W11MIN} - X_o)^2 + (Y_{W1MAX} - Y_o)^2} = 1 \quad (11)$$

$$(\varepsilon_2): \frac{(X - X_o)^2 + (Y - Y_o)^2}{(X_{W11MAX} - X_o)^2 + (Y_{W1MIN} - Y_o)^2} = 1 \quad (12)$$

$$(\varepsilon_1'): \frac{(X - X_o')^2 + (Y - Y_o)^2}{(X_{W1MAX} - X_o')^2 + (Y_{W1MAX} - Y_o)^2} = 1 \quad (13)$$

$$(\varepsilon_2'): \frac{(X - X_o')^2 + (Y - Y_o)^2}{(X_{W1MIN} - X_o')^2 + (Y_{W1MIN} - Y_o)^2} = 1 \quad (14)$$

The equation describing K_z is of the form of (15). The ellipse symbols appearing in (15) refer to the left hand side of (11)–(14),

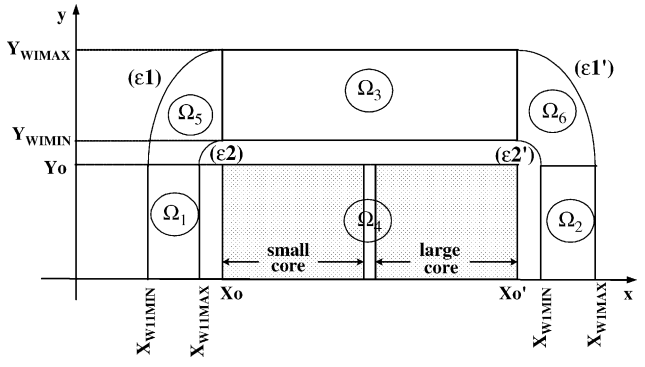

Fig. 8. Regions (xy-plane) of the subdomain used in the calculation of the fictitious field distribution K_z corresponding to the LV winding (elliptical approximation of the winding corners).

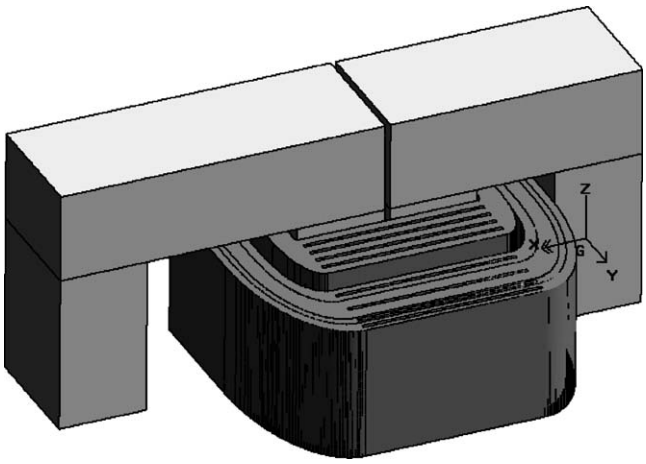

Fig. 9. Perspective view of the active part of the transformer one phase part modeled (detailed winding geometry).

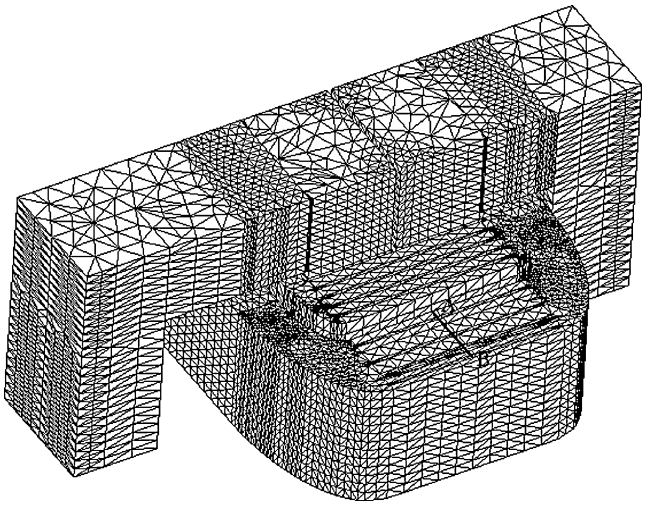

Fig. 10. Tetrahedral finite element mesh representing the transformer active part (detailed winding geometry).

an expression that was chosen for the sake of simplicity.

$$K_z = \begin{cases} \mathrm{NI}\cdot Z\cdot \dfrac{X_{\mathrm{W11MIN}} - X}{X_{\mathrm{W11MIN}} - X_{\mathrm{W11MAX}}}, & \text{region } \Omega_1 \\ \mathrm{NI}\cdot Z\cdot \dfrac{X_{\mathrm{W1MAX}} - X}{X_{\mathrm{W1MAX}} - X_{\mathrm{W1MIN}}}, & \text{region } \Omega_2 \\ \mathrm{NI}\cdot Z\cdot \dfrac{Y_{\mathrm{W1MAX}} - Y}{Y_{\mathrm{W1MAX}} - Y_{\mathrm{W1MIN}}}, & \text{region } \Omega_3 \\ \mathrm{NI}\cdot Z, & \text{region } \Omega_4 \\ \mathrm{NI}\cdot Z\cdot \dfrac{(\varepsilon_1) - 1}{(\varepsilon_1) - (\varepsilon_2)}, & \text{region } \Omega_5 \\ \mathrm{NI}\cdot Z\cdot \dfrac{(\varepsilon_1') - 1}{(\varepsilon_1') - (\varepsilon_2')}, & \text{region } \Omega_6 \end{cases} \tag{15}$$

Eq. (15) derived under the assumption that the current flows through the whole area of the considered winding. This assumption does not take into account the existence of cooling ducts in the winding area outside the core windows, where the current density is in fact equal to zero, because of the oil flowing through them. This approximation consists another factor of the magnetic field overestimation, as it increases the magnetic field sources area. Therefore, the existence of cooling ducts must be inserted into the analysis in order to obtain more reliable results.

Fig. 9 shows the perspective view of the transformer model with detailed representation of the transformer windings, including the cooling ducts. The modeling of ducts affects the calculation of the fictitious field distribution K_z as well as the construction of the finite element mesh of the transformer active part, shown in Fig. 10.

With respect to Fig. 8, the ducts are located in the region Ω_3 of the winding; thus, the distribution must be recalculated in this region only. The new bottom view of both LV and HV windings is shown in Fig. 11. The LV winding comprises four cooling ducts while each one of the HV subcoils comprises one cooling duct. All the ducts have the same thickness, equal to W_{DUCT}.

The region Ω_3 of the LV winding is divided into nine sub-regions: five "winding" sub-regions and four "duct" sub-regions. Fig. 12 gives a detailed description of the coordinates of each sub-region boundary coordinates (along xy-plane) and the way they are connected inside each winding area. In the case of the LV winding, the four ducts are placed symmetrically in the center of region Ω_3, dividing the region into nine sub-regions: since the width of each "duct" sub-region is equal to W_{DUCT}, the width of remaining five "winding" sub-regions is equal to the width of the LV winding inside the core windows, divided to five (i.e. the number of the "winding" sub-regions). Similarly, in the case of the HV1 subcoil, the single existent duct is placed in the center of the respective region Ω_3, dividing the region into three sub-regions: therefore, the width of the "duct" sub-region is equal to W_{DUCT} and the width of remaining two "winding" sub-regions is equal to the width of the HV1 subcoil inside the core windows, divided to two (i.e. the number of the "winding" sub-regions). The definition of the coordinates of Fig. 12 may be used as a general criterion for the definition of the winding area subdivision into sub-regions. In cases where the number of LV winding ducts is not equal to four or the number of HV winding ducts is not equal to one per subcoil, the geometrical parameters remain the same, as long as an equivalent duct width $W_{\mathrm{DUCT}}^{\mathrm{LV}}$, $W_{\mathrm{DUCT}}^{\mathrm{HV}}$ is chosen for the LV and HV winding, respectively, according to the following relationships:

$$W_{\mathrm{DUCT}}^{\mathrm{LV}} = \frac{N_{\mathrm{DUCT}}^{\mathrm{LV}}\cdot W_{\mathrm{DUCT}}}{4} \tag{16}$$

$$W_{\mathrm{DUCT}}^{\mathrm{HV}} = N_{\mathrm{DUCT}}^{\mathrm{HV}}\cdot W_{\mathrm{DUCT}} \tag{17}$$

where $N_{\mathrm{DUCT}}^{\mathrm{HV}}$, $N_{\mathrm{DUCT}}^{\mathrm{LV}}$ are the number of LV and HV winding ducts, respectively.

The distribution K_z of the region Ω_3 corresponding to the LV winding has the form of Fig. 13, which shows the K_z distribution along a plane parallel to y-axis, crossing the center X_c of the winding (similar to Fig. 6).

The equation of distribution K_z for region Ω_3 of LV winding (Fig. 12) is given by (18). The first branch of (18) refers to the "winding" sub-regions, while the second branch refers to the

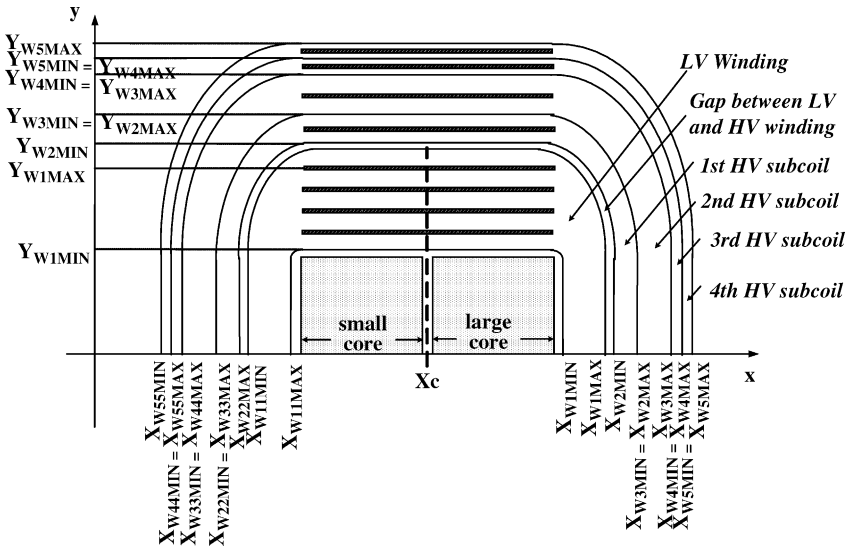

Fig. 11. Division of the windings used in the representation of cooling ducts (*xy*-plane).

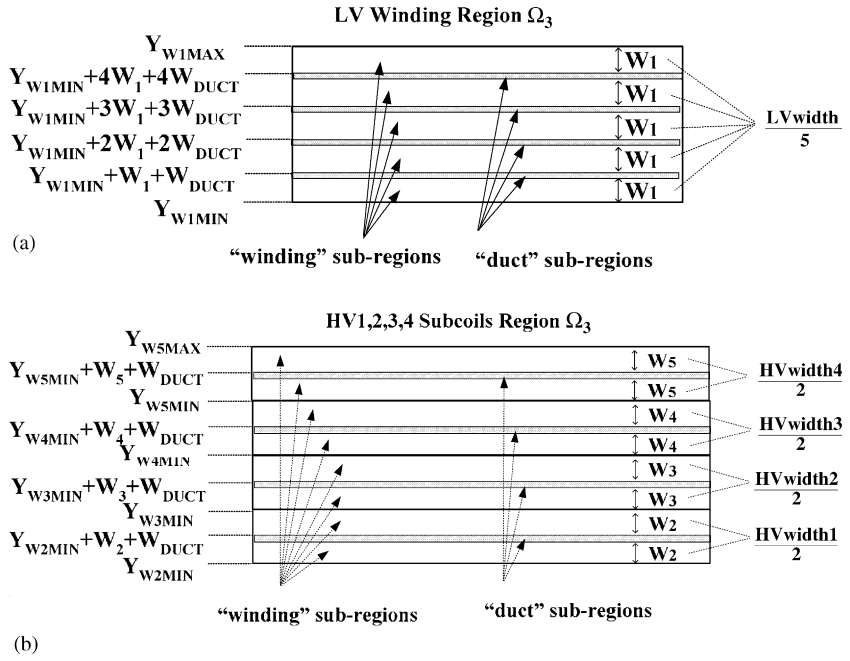

Fig. 12. Geometrical criteria for the windings area division in "ducts" and "winding" sub-regions (*xy*-plane). (a) LV winding and (b) HV subcoils.

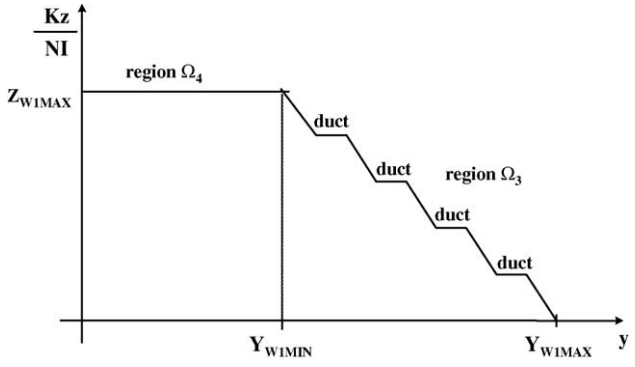

Fig. 13. Fictitious field distribution corresponding to the LV winding along the plane $X = X_c$ of Fig. 11 (similar to Fig. 6 with consideration of cooling ducts).

"duct" sub-regions.

$$\frac{K_z}{\mathrm{NI}\cdot Z}=\begin{cases}-\dfrac{1}{5\cdot W_1}[Y+Y_{\mathrm{W1MIN}}+j\cdot W_1+(j-1)\\ \quad\cdot W_{\mathrm{DUCT}}]+\dfrac{|j-5|}{5}, & j=1,\ldots,5\\ \dfrac{|j-5|}{5}, & j=1,\ldots,4\end{cases}\tag{18}$$

where W_1 is the width of each "winding" sub-region, given by:

$$W_1=\frac{\mathrm{LVWidth}}{5}\tag{19}$$

where LVWidth is the width of the LV winding inside the core windows.

Similarly, the region Ω_3 of the first HV subcoil is divided into three sub-regions: two "winding" sub-regions and one "duct" sub-region. The respective equation for K_z is:

$$\frac{K_z}{\mathrm{NI}\cdot Z} = \begin{cases} -\dfrac{1}{3\cdot W_2}[Y + Y_{\mathrm{W2MIN}} + j\cdot W_2 + (j-1)\cdot \\ \quad W_{\mathrm{DUCT}}] + \dfrac{|j-3|}{3}, \quad j = 1,\ldots,3 \\ \dfrac{|j-3|}{3}, \quad j = 1 \end{cases} \tag{20}$$

where W_2 is the width of each "winding" sub-region, given by:

$$W_2 = \frac{\mathrm{HVWidth1}}{3} \tag{21}$$

where HVWidth1 is the width of the first HV subcoil inside the core windows.The first branch of (20) refers to "winding" sub-regions, while the second one corresponds to the "duct" sub-region. The form of the equations for K_z of the next three HV subcoils are identical to (21) with the respective boundaries along x-, y- and z-axes.

The construction of the mesh appearing in Fig. 10 can be realized through a commercial tool for mesh construction. In the considered transformer model, an initial 2D mesh was constructed, along the xy-plane of the model. Consequently, mesh edges, including the subdivisions on the edges, were propagated throughout the entire mesh in the sweep direction (i.e. the transformer model height along z-axis). The meshing tolerance was less than 1% of the smallest edge length of the model, in order to avoid mesh distortion problems. For the construction of the initial 3D mesh, first-order tetrahedral elements were used. Although the use of higher order elements was possible, it was not implemented in the pre-processor, as they did not contribute to the increase of the model accuracy, while they resulted to greater computation time. As the construction of the initial mesh was crucial for the accuracy of the calculations conducted by the finite element method, careful consideration was given on its density and homogeneity. Moreover, as the computation time increases with the number of mesh nodes, the total mesh size should be confined below a number that guarantees a not excessively time consuming solution model. For this purpose, meshes of various densities were constructed, after refinement in areas of special interest: that is why the nodes density in the mesh of Fig. 10 is greater in the windings area (especially in the winding corners), in order to obtain greater accuracy in the magnetic field sources region. The optimum number of elements was chosen after the comparison of the results in different transformer cases, as it is described in the following section.

3. Results and discussion

3.1. Local field values

The field values computed by the proposed 3D FEM model (detailed winding geometry) have been compared to those measured by a Hall effect probe during short-circuit test. Figs. 14 and 15 give the variation of the perpendicular flux density component B_n along the line AB, positioned as shown in Fig. 10, in case of short-circuit with the high voltage winding connections corresponding to 20 and 15 kV voltage supply. These figures illustrate the good correlation of the simulated results with the local leakage field measured by Hall effect probes.

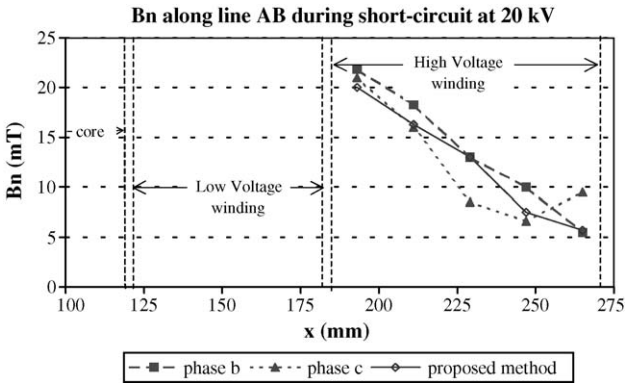

Fig. 14. Comparison of measured and computed field values along the line AB during short-circuit at 20 kV.

3.2. Short-circuit impedance

The finite element method results were used to calculate the transformer short-circuit impedance. Both models with simplified and detailed winding geometry were used.

The results were compared with the short-circuit impedance measured after the transformer construction. Figs. 16 and 17 show the deviation of the calculated short-circuit impedance from the measured one for different mesh densities of the two models used in the case of the first (20 kV) and second (15 kV) primary voltage level.

The results of Figs. 16 and 17 are tabulated in Tables 1 and 2. The deviation appearing in these tables is defined by:

$$\text{deviation}\,(\%) = \frac{|U_k^{\text{calculated}} - U_k^{\text{measured}}|}{U_k^{\text{measured}}}\cdot 100\% \tag{22}$$

where $U_k^{\text{calculated}}$ is the short-circuit impedance calculated with the use of the FEM model, while U_k^{measured} is the measured short-circuit impedance value.

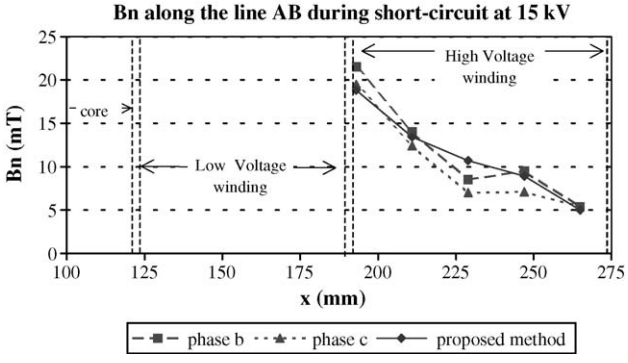

Fig. 15. Comparison of measured and computed field values along the line AB during short-circuit at 15 kV.

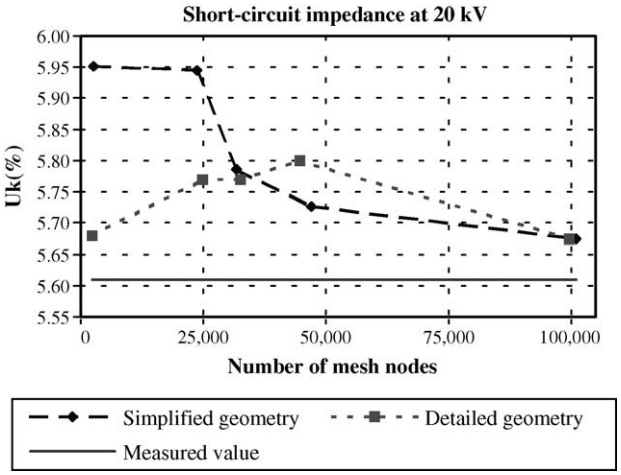

Fig. 16. Short-circuit impedance results (primary voltage 20 kV) for simplified and detailed winding geometry.

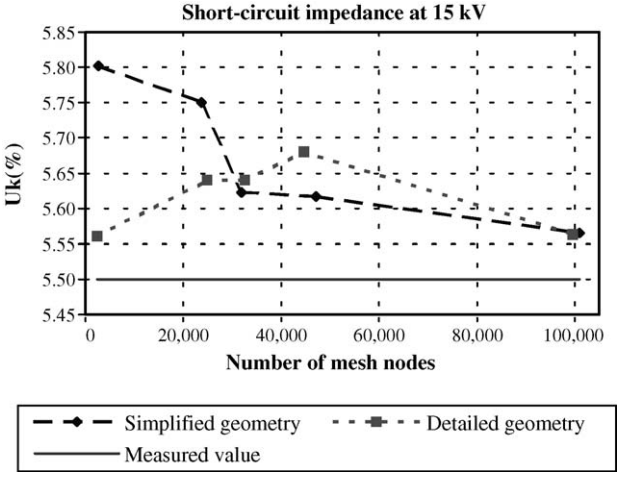

Fig. 17. Short-circuit impedance results (primary voltage 15 kV) for simplified and detailed winding geometry.

The comparison of the curves shown in Figs. 16 and 17 leads to the following conclusions:

(1) The error in the calculation of the short-circuit impedance with the use of the detailed winding geometry model begins from a very small value for a sparse mesh (instead of the great error given by the simplified geometry model) and rises with the increase of the number of mesh nodes. This may be attributed to the fact that detailed geometry representation by using small number of unknowns leads to some kind of compensating errors for the source field representation.
(2) At an intermediate mesh density (30,000 nodes approximately) the error of the detailed model approaches the one of the simplified model.
(3) The two models converge to the same error at high mesh densities (beyond 90,000 nodes).
(4) The variation of the error is similar for the two high voltage levels.
(5) The minimum deviation appearing in Tables 1 and 2 is less than 1.5%, obtained with the use of detailed winding model, for both first (lowest) and last (highest) mesh density and with the use of the simplified winding model for the larger number of nodes.

Table 1
Short-circuit impedance results for simplified winding geometry

Primary voltage level (kV)	Number of mesh nodes	$U_k^{calculated}$ (%)	$U_k^{measured}$ (%)	Deviation (%)
20	2613	5.97	5.61	6.42
	23696	5.95		6.06
	31818	5.77		2.85
	47044	5.73		2.14
	100999	5.67		1.07
15	2613	5.82	5.50	5.82
	23696	5.75		4.55
	31818	5.63		2.36
	47044	5.62		2.18
	100999	5.57		1.27

Table 2
Short-circuit impedance results for detailed winding geometry

Primary voltage level (kV)	Number of mesh nodes	$U_k^{calculated}$ (%)	$U_k^{measured}$ (%)	Deviation (%)
20	3260	5.69	5.61	1.43
	24862	5.77		2.85
	32555	5.77		2.85
	44660	5.80		3.39
	99567	5.67		1.07
15	3260	5.56	5.50	1.09
	24862	5.65		2.73
	32555	5.63		2.36
	44660	5.68		3.27
	99567	5.57		1.27

In order to validate the above conclusions, the same analysis was conducted for two more cases of transformers of rated primary voltage 20 and 15 kV, rated secondary voltage 400 V and rated power 400 and 1000 kVA. Figs. 18 and 19 give the respective error curves in the short-circuit impedance calculation, with the use of the simplified and the detailed model, at 20 kV. The shape of the error curves is similar to the one of Figs. 16 and 17, as the greater accuracy is achieved in the lowest mesh density for the detailed model in both cases.

The detailed model of the winding geometry is therefore appropriate for a very accurate calculation of the short-circuit impedance with the use of a sparse mesh. This ability is quite important for the finite element method as it overcomes one of its main drawbacks, consisting in the computational time required for obtaining reliable results.

3.3. Generalization of results

The proposed methodology has proven to be cost effective and quite accurate in the prediction of the leakage field and the short-circuit impedance of the transformer examined in Section 2. However, further work was necessary to enable its implementation in several three-phase dual voltage wound core

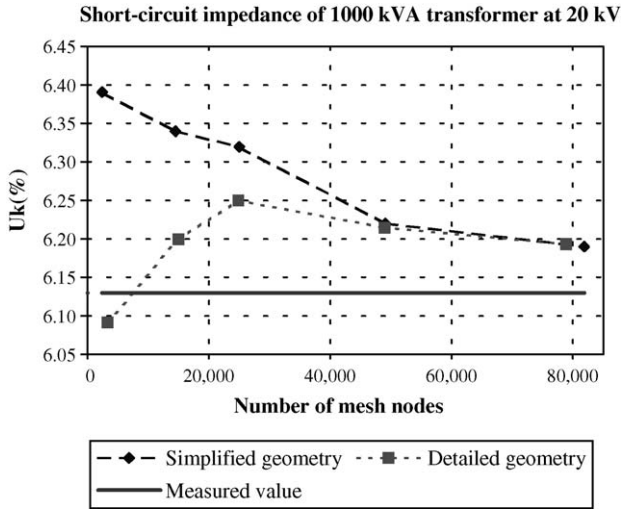

Fig. 18. Short-circuit impedance results (primary voltage 20 kV) for the 1000 kVA transformer (simplified and detailed windings geometry).

transformers. The design of dual voltage transformers is of special interest, as their windings are arranged in specific ways and their characteristics may vary widely with the change in connection, depending on winding arrangement [19]. Therefore, accurate calculation techniques as the finite element analysis for both connections must be conducted to ensure reliable performance and to maintain design margins during short-circuit and other transient phenomena [20].

For the above purpose, a computer code was developed, performing the finite element calculations that provide the value of the short-circuit impedance. A process of mesh parameterization was adopted, which modifies the coordinates of initial tetrahedral meshes of various densities in accordance with the geometric data of the examined transformers. In this way, the program user does not interfere with three-dimensional model construction, a time-consuming procedure that demands specific computer aided design knowledge. This interface has overbalanced another major deficiency that has so far restrained the proliferation of the use of 3D FEM techniques in the transformer

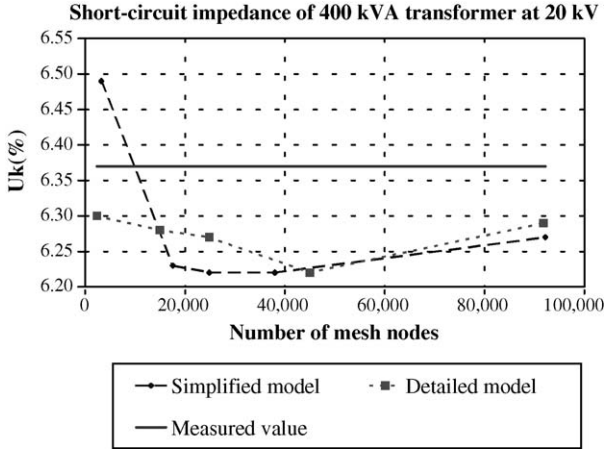

Fig. 19. Short-circuit impedance results (primary voltage 20 kV) for the 400 kVA transformer (simplified and detailed windings geometry).

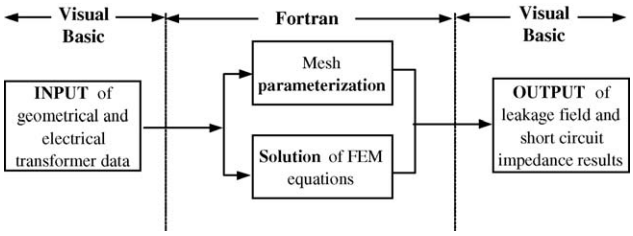

Fig. 20. Structure of the computer code implemented for the calculation of the transformer short-circuit impedance.

manufacturing industry. The structure of the computer program is depicted in the flowchart of Fig. 20.

The main concept of the parameterization process relies on the modification of dimensions of existing meshes (constructed from an initial transformer model, which can derive through an automated pre-processing commercial tool, as stated in Section 2.4) according to the geometrical data of each considered transformer. This is realized by alteration of the mesh nodal coordinates with the use of equations deriving from the transformer geometry.

For the simplification of the parameterisation process, the initial meshes were divided into multiple regions. The division was based on the dimensions affecting the nodes of each region: thus, an effort was made to group neighboring nodes whose coordinates depend on the variation of the same transformer geometrical parameters into simply connected regions. This procedure resulted to 84 regions, whose perspective view is shown in Fig. 21.

The initial meshes are integrated to the program input data in the form of ASCII files. An identification number (ID) is assigned to each node and element of the mesh, while the material property of each element is represented by a number. This method allows the program to identify the region where each element belongs and the coordinates of its vertices with the use

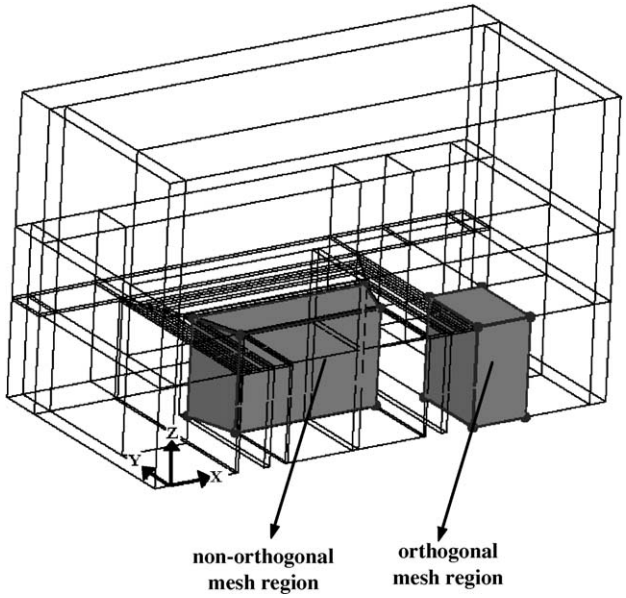

Fig. 21. Perspective view of the transformer model division to regions during the mesh parameterization process.

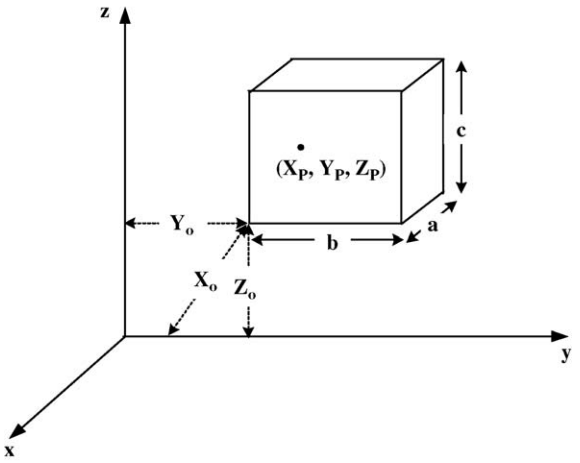

Fig. 22. Orthogonal mesh region.

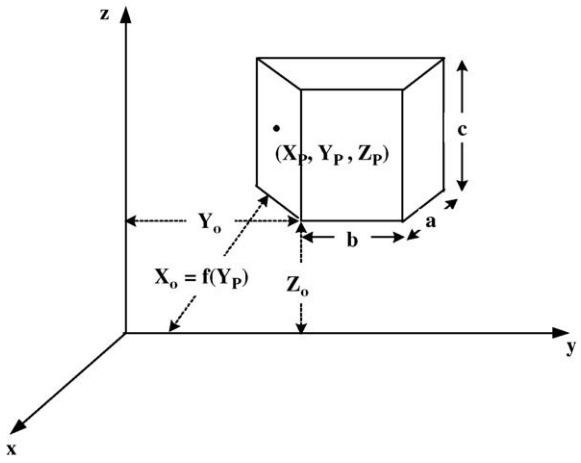

Fig. 23. Non-orthogonal mesh region.

of the ID values stored in the nodes and elements arrays during the reading of input data. The vertices nodes of the elements are stored in a Nelem × 4 array, where Nelem is the total number of mesh elements. The material of each element is stored in a Nelem × 1 array. The material of each mesh region is represented by an integer $k \in [1–84]$. The parameterized mesh derives from modification of the mesh nodal coordinates, described in the followings.

Let us consider an orthogonal mesh region, shown in Fig. 22, where (X_P, Y_P, Z_P) are the coordinates of a random point inside the region, (a, b, c) are the dimensions of the region along x-, y- and z-axes while (X_o, Y_o, Z_o) are the distances of the region origin from the Cartesian coordinate system origin. A change in the model dimensions will affect the dimensions (a, b, c) as well as the distances (X_o, Y_o, Z_o). The new coordinates of point P will derive from (23). In this equation, the superscripts "old" refer to the old (initial) coordinates, while the superscripts "new" refer to the new coordinates (after the change of the transformer dimensions).

$$\begin{cases} X_P^{new} = \dfrac{a^{new}}{a^{old}}(X_P^{old} - X_o^{old}) + X_o^{new} \\ Y_P^{new} = \dfrac{b^{new}}{b^{old}}(Y_P^{old} - Y_o^{old}) + Y_o^{new} \\ Z_P^{new} = \dfrac{c^{new}}{c^{old}}(Z_P^{old} - Z_o^{old}) + Z_o^{new} \end{cases} \quad (23)$$

The procedure is similar for a non-orthogonal mesh region and the only difference relies on the fact that dimensions (a, b, c) and (X_o, Y_o, Z_o) are not constant and depend on the coordinates of the examined point P. For example, in the region of Fig. 23, the distance X_o is function of the y-coordinate of point P. In this case, X_o can be easily calculated with the use of the line equation of the region edge, which derives from the region boundaries.

The magnetic scalar potential at each mesh node is calculated by solution of the discretized form of the differential equation governing the magnetostatic problem. The solution is implemented in the developed FEM software solver with the use of an efficient iterative algorithm (preconditioned conjugate gradient), as it is more efficient in the aspect of less memory requirement, less computational amount and less round off error. After the solution of the FEM system of equations, the transformer short-circuit impedance derives with the use of the resulting magnetic energy of the model which is used to calculate the total windings leakage inductance and the resulting inductive voltage drop.

The use of the detailed geometry model of the transformer, described in Section 2.4 enables the representation of transformers of different power ratings and voltage levels in the primary winding. Single or dual primary voltage transformers can be modeled. The windings connection (delta, star or zig-zag) does not affect the model characteristics. The initial division of the HV winding area into four sub-regions was selected in purpose, as it can also model other possible winding arrangements for dual primary voltage production, apart from the one described in Fig. 3. Each HV winding arrangement is represented in the model by assigning the appropriate current to each HV subcoil, according to the examined primary voltage level. The calculation of the fictitious field distribution **K** corresponding to each winding is then calculated as described in Section 2.4, taking proper account of the number of LV and HV winding ducts.

An alternative way of obtaining dual primary voltage 20–15 kV is shown in Fig. 24. In this case, the two intermediate HV subcoils (HV2 and HV3) are connected in parallel and then in series with the rest two subcoils (HV1 and HV4), in order to obtain the second HV level (15 kV). Therefore, to model this connection, one needs to consider that the current flowing through HV2 and HV3 is half of the current flowing through HV1 and HV4.

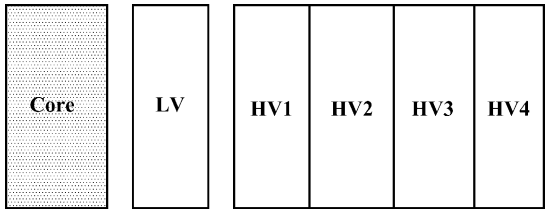

Fig. 24. Alternative winding arrangement (yz-plane) for the production of dual primary voltage levels 20–15 kV.

Table 3
Application of the proposed method to several transformer cases

	Rating (kVA)	Primary voltage level (kV)	$U_k^{\text{calculated}}$ (%)	U_k^{measured} (%)	Deviation (%)
1	1000	20	6.26	6.27	0.16
		15	6.30	6.17	2.06
2	630	20	3.83	3.77	1.57
		6.6	3.81	3.75	1.57
3	400	20	6.37	6.22	2.35
		15	6.08	5.95	2.14
4	100	33	4.14	4.09	1.21
5	100	20	4.27	4.16	2.58
		15	4.19	4.17	0.48

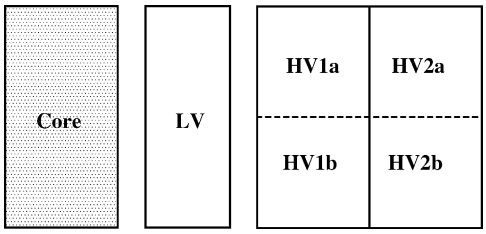

Fig. 25. Winding arrangement (*yz*-plane) for the production of dual primary voltage levels 20–10 kV.

Fig. 25 illustrates a HV winding arrangement that gives dual primary voltage 20–10 kV. In this case, the HV winding is divided into two subcoils only (HV1 and HV2), which consist of two sections (HV1a–HV1b and HV2a–HV2b), connected in parallel for the production of the lower HV level (10 kV). Consequently, at primary voltage level equal to 10 kV, subcoils HV1 and HV2 carry half of the nominal current. In order to model the connection described above, the four HV winding sub-regions of the FEM model of Fig. 9 are arranged as follows: the first two sub-regions represent subcoil HV1, while the two last sub-regions represent subcoil HV2.

In Fig. 26, an arrangement that produces dual primary voltage level 20-6.6 kV is shown. This arrangement resembles to the one of Fig. 25, besides the fact that HV1 and HV2 are divided into three sections. Thus, at primary voltage level equal to 6.6 kV, one third of the nominal current flows through HV1 and HV2.

Table 3 summarizes the results of the calculated short-circuit impedance values in five cases along with the ones measured after the transformers construction. The secondary voltage levels of the transformers are equal to 400 V, except for transformer 4, whose nominal secondary voltage is equal to 433 V. The computed results compare favorable with the measured values, as the difference between them appears to be less than 2.5% in most of the cases. The maximum deviation is equal to 2.64% while the minimum one is less than 0.5%.

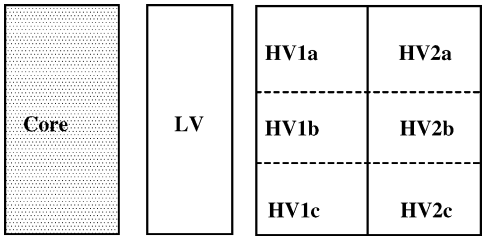

Fig. 26. Winding arrangement (*yz*-plane) for the production of dual primary voltage levels 20–6.6 kV.

Table 4
FEM solution times for different mesh densities

Number of mesh nodes	Solution time (min) for Pentium 4, 2.4 GHz, 512 MB RAM
3260	1.5
23696	20
32555	35
55473	140
89603	190

The calculations were conducted with the detailed transformer model and a sparse mesh of approximately 3500 nodes. As the accuracy provided by a sparse mesh is equivalent to the one of a mesh of several thousands of nodes, it can be used systematically in the short-circuit impedance evaluation. Table 4 compares the solution times required for different mesh densities in the case of an average performance personal computer. The use of a coarse mesh density reduces the solution time to a few minutes, enabling the employment of the method in an automated transformer design process.

4. Conclusions

An efficient 3D FEM model of power transformers for the leakage field and short-circuit impedance evaluation, suitable for design office use, has been developed and applied in the transformer manufacturing industry. The detailed representation of the transformer (focusing on the winding geometry and cooling ducts) and the particular reduced scalar potential technique adopted consist the main advantages of the model, with respect to standard FEM codes. It has been validated through local field measurements and short-circuit impedance calculation in several three-phase, wound core, single and dual voltage, power transformers. The computed results compared favorable to the measured values and the mean deviation in the impedance value was less than 3%. The method is very cost effective, as high

accuracy is obtained for low mesh densities, requiring little computational time. This ability, along with the development of an automated, user-oriented, transformer short-circuit impedance calculation program based on the FEM model overcome the main deficiencies of the method and enable its use during the preliminary design process.

Acknowledgement

This work was supported in part by the General Secretariat for Research and Technology of Greece under PAVET Grant No. 00BE457.

References

[1] P.S. Georgilakis, N.D. Doulamis, A.D. Doulamis, N.D. Hatziargyriou, S.D. Kollias, A novel iron loss reduction technique for distribution transformers based on a combined genetic algorithm-neural network approach, IEEE Trans. Syst. Man Cybernet. Part C: Appl. Rev. 31 (1) (2001) 16–34.
[2] P. Georgilakis, N. Hatziargyriou, D. Paparigas, AI helps reduce transformer iron losses, IEEE Comput. Appl. Power 12 (4) (1999) 41–46.
[3] IEC 60076-1, Power transformers—Part 1: General, 2000.
[4] K. Shima, K. Ide, M. Takahashi, Y. Yoshinari, M. Nitobe, Calculation of leakage inductances of a salient-pole synchronous machine using finite elements, IEEE Trans. Energy Convers. 14 (4) (1999) 1156–1161.
[5] S. Williamson, D.R. Gersh, Finite element calculation of double-cage rotor equivalent circuit parameters, IEEE Trans. Energy Convers. 11 (1) (1996) 41–48.
[6] T.F. Chan, L.L. Lai, Lie-Tong Yan, Finite element analysis of a single-phase grid-connected induction generator with the steinmetz connection, IEEE Trans. Energy Convers. 18 (2) (2003) 321–329.
[7] F. Colamartino, C. Marchand, A. Razek, Torque ripple minimization in permanent magnet synchronous servodrive, IEEE Trans. Energy Convers. 14 (3) (1999) 616–621.
[8] D. Pavlik, V.K. Garg, J.R. Repp, J. Weiss, A finite element technique for calculating the magnet sizes and inductances of permanent magnet machines, IEEE Trans. Energy Convers. 3 (1) (1998) 116–122.
[9] M. Moallem, C.M. Ong, Predicting the torque of a switched reluctance machine from its finite element field solution, IEEE Trans. Energy Convers. 5 (4) (1990) 733–739.
[10] C. Xiang, Y. Jinsha, Z. Guoquiang, Z. Yuanlu, H. Qifan, Analysis of leakage magnetic problems in shell-form power transformer, IEEE Trans. Magn. 33 (2) (1997) 2049–2051.
[11] G.F. Mechler, R.S. Girgis, Calculation of spatial loss distribution in stacked power and distribution transformer cores, IEEE Trans. Power Deliv. 13 (2) (1998) 532–537.
[12] A.G. Kladas, M.P. Papadopoulos, J.A. Tegopoulos, Leakage flux and force calculation on power transformer windings under short-circuit: 2D and 3D models based on the theory of images and the finite element method compared to measurements, IEEE Trans. Magn. 30 (5/2) (1994) 3487–3490.
[13] O. Mohammed, N. Demerdash, A 3-D finite element perturbational method for determining saturated values of transformer winding including experimental verification, IEEE Trans. Magn. 21 (5) (1985) 1877–1879.
[14] M. Enokizono, N. Soda, Finite element analysis of transformer model core with measured reluctivity tensor, IEEE Trans. Magn. 33 (5) (1997) 4110–4112.
[15] S. Bouissou, F. Piriou, C. Kieny, G. Tanneau, Numerical simulation of a power transformer using 3D finite element method coupled to circuit equation, IEEE Trans. Magn. 30 (5) (1994) 3224–3227.
[16] A.A. Arkadan, R.H. VanderHeiden, Three-dimensional nonlinear finite element modeling of a voltage source excited transformer feeding a rectifier load, IEEE Trans. Magn. 28 (5) (1992) 2265–2267.
[17] M.A. Tsili, A.G. Kladas, P.S. Georgilakis, A.T. Souflaris, C.P. Pitisilis, J.A. Bakopoulos, D.G. Paparigas, Hybrid numerical techniques for power transformer modeling: a comparative analysis validated by measurements, IEEE Trans. Magn. 40 (2) (2004) 842–845.
[18] A. Kladas, J. Tegopoulos, A new scalar potential formulation for 3D magnetostatics necessitating no source field calculation, IEEE Trans. Magn. 28 (1992) 1103–1106.
[19] J.A. Ebert, Criteria for reliable dual voltage power transformers, IEEE Trans. Power Deliv. 10 (2) (1995) 845–852.
[20] S.H. Digby, H.J. Sim, Transformer design for dual-voltage applications, in: IEEE Rural Electric Power Conference, A1-A1_9, May, 2002.

Marina A. Tsili (S'04) was born in Greece, in 1976. She received the diploma in electrical and computer engineering from the National Technical University of Athens in 2001 where she follows post-graduate studies. Her research interests include transformer and electric machine modeling as well as analysis of generating units by renewable energy sources.

Antonios G. Kladas was born in Greece, in 1959. He received the diploma in electrical engineering from the Aristotle University of Thessaloniki, Greece in 1982 and the D.E.A. and Ph.D. degrees in 1983 and 1987, respectively, from the University of Pierre and Marie Curie (Paris 6), France. He served as associate assistant in the University of Pierre and Marie Curie from 1984 to 1989. During the period 1991–1996, he joined the Public Power Corporation of Greece, where he was engaged in the System Studies Department. Since 1996 he joined the Department of Electrical and Computer Engineering of the National Technical University of Athens (NTUA), where he is now associate professor. His research interests include transformer and electric machine modeling and design as well as analysis of generating units by renewable energy sources and industrial drives.

Pavlos S. Georgilakis (S'98, M'01) was born in Chania, Greece in 1967. He received the diploma in electrical and computer engineering and the Ph.D. degree from the National Technical University of Athens, Greece in 1990 and 2000, respectively. From 1994 to 2003 he was with Schneider Electric AE, where he worked as quality control engineer for 1 year, transformer design engineer for 4 years, R&D manager for 3 years and low voltage products marketing manager for 2 years. He is currently assistant professor at the Production Engineering and Management Department of the Technical University of Crete (TUC) and Director of Electric Circuits and Electronics Laboratory. His research interests include transformer modeling and design as well as power systems and intelligent systems. He is member of IEEE, CIGRE, and the Technical Chamber of Greece.

Athanasios T. Souflaris was born in Athens, Greece in 1956. He received the diploma in electrical engineering from the Technical University of Pireaus, Greece in 1981. He joined Schneider Electric AE in 1985 as transformer design engineer and from 1988 he is the transformer design manager of Schneider Electric AE.

Dimitrios G. Paparigas was born in Komotini, Greece in 1945. He received the diploma in electric machines and instruments from the Moscow Energy Institute, U.S.S.R. in 1972. From 1974 to 1976, he worked in the Engineering Department of Masina Xrisolouris, Greece. Since 1976, he has been with Schneider Electric AE (former Elvim), Greece. He has been engaged in several positions, such as quality control manager, production manager, transformer design manager and quality assurance Director. At present, he is technical division Director and industrial division Director.